Journal of Power Sources 227 (2013) 318–326

Contents lists available at SciVerse ScienceDirect

Journal of Power Sources

journal homepage: www.elsevier.com/locate/jpowsour

Formation of spinel reaction layers in manganese cobaltite – coated Crofer22 APU for solid oxide fuel cell interconnects

Neal J. Magdefrau [a,*], Lei Chen [a], Ellen Y. Sun [a], Jean Yamanis [a], Mark Aindow [b]

[a] United Technologies Research Center, Physical Sciences, 411 Silver Lane, East Hartford, CT 06108, USA
[b] Department of Chemical, Materials and Biomolecular Engineering, and Institute of Materials Science, University of Connecticut, Storrs, CT 06269, USA

HIGHLIGHTS

- Manganese cobaltite coated Crofer22 APU has been examined by transmission electron microscopy.
- As-coated samples exhibit thin Co/Cr-rich spinel reaction layers at alloy/coating interfaces.
- Oxidation in air for up to 1000 h causes chromia subscale formation and changes in spinel layers.
- Spinel layer development is related to changes in diffusive fluxes during coating and oxidation.

ARTICLE INFO

Article history:
Received 30 April 2012
Received in revised form
25 July 2012
Accepted 30 July 2012
Available online 14 August 2012

Keywords:
Solid oxide fuel cell interconnects
Manganese cobaltite coatings
Microstructure
Reaction layer
Electron microscopy

ABSTRACT

The microstructural development of $Mn_{1.5}Co_{1.5}O_4$-coated Crofer22 APU has been studied using cross-sectional transmission electron microscopy. Alloy samples were coated via a slurry process involving consolidation by reduction and re-oxidation, and these samples were then oxidized at 800 °C for times of up to 1000 h. All samples exhibited a thin chromia scale at the alloy/coating interface plus spinel phases as a reaction layer between the chromia and the manganese cobaltite coating. The oxidized samples also exhibited pockets of stoichiometric $MnCr_2O_4$ spinel at the chromia/alloy interface and internal Ti-rich oxides in the alloy below the chromia. The reaction layer spinels exhibit remarkable changes in thickness, morphology and composition, and these effects are explained on the basis of changes in the diffusive fluxes during the different stages of coating application and subsequent exposure. The possible consequences of these observations for the degradation mechanisms that could affect SOFC interconnects produced from MCO-coated Crofer22 APU are discussed.

1. Introduction

Solid Oxide Fuel Cells (SOFCs) have the potential to play an important role in the future of power generation due to their fuel flexibility and high system efficiencies. Recent progress in manufacturing thinner electrolyte layers has enabled SOFC operating temperatures to be reduced from 1000 °C to 600–800 °C. One benefit of this reduced operating temperature is that stack components such as interconnects, which had previously been made of expensive ceramic materials, can now be replaced by metallic components. Metallic interconnects are attractive due to their low cost, high electrical conductivity and high formability, which makes them easy to manufacture on a large scale. Most of the interconnect materials currently under consideration are iron- or nickel-based alloys that contain chromium and form a protective, semi-conductive chromia scale as an oxidation product. Unfortunately, exposure of chromia scales in air at elevated temperatures during SOFC operation causes the formation of volatile $CrO_2(OH)_2$ and CrO_3, leading to poisoning of the cathode materials [1–3]. Thus, current SOFC interconnect alloys require protective coatings that suppress the formation of these volatile chromia species [4,5].

The most successful coatings to date have been based on manganese cobaltite ($(Mn,Co)_3O_4$ – MCO), which inhibits chromia volatility while simultaneously slowing the oxidation kinetics of the base alloy (e.g. [6]). The most widely studied MCO composition is $Mn_{1.5}Co_{1.5}O_4$; it has been shown that coatings with this stoichiometry exhibit two-phase microstructures (comprising cubic $MnCo_2O_4$ and tetragonal Mn_2CoO_4 spinel phases) and electrical conductivities of >60 S cm^{-1} at 800 °C [7,8]. Such MCO spinel coatings are typically applied as a slurry followed by a two-step (reduction/oxidation) reactive sintering process. However, slurry-

* Corresponding author. Tel.: +1 860 610 7403; fax: +1 860 660 4512.
E-mail address: magdefnj@utrc.utc.com (N.J. Magdefrau).

0378-7753/$ – see front matter © 2012 United Technologies Corporation. Published by Elsevier B.V. All rights reserved.
http://dx.doi.org/10.1016/j.jpowsour.2012.07.091

processed coatings tend to be rather porous, and there has been a recent push to develop denser coatings by electrodeposition of metallic layers followed by oxidation to form the spinel phases [9–11]. Other groups have attempted to tailor the MCO chemistry by introducing substitutional cations into the spinel structure to increase the densities and/or electrical conductivities of the coatings [12,13]. Experimental results from Pacific Northwest National Laboratory (PNNL) have confirmed that low-level (<1 atomic%) additions of rare earth elements such as cerium to the MCO coating improved the chromia scale adhesion on ferritic stainless steel substrates [14]. This is particularly important for long-term durability as experimental tests indicate that the chromia/alloy interface may be mechanically weaker than the chromia/coating interface [15]. Ce-modified MCO coated stainless steel 441 exhibits an acceptably low and stable area specific resistance (ASR) after >15,000 h of exposure at 800 °C [16].

A major concern for any such high-temperature coating system is the possibility of reaction layers (RLs) forming between the coating and the alloy or the chromia sub-scale. Since the electrical and mass transport properties of such RLs could be rather different from those of the coating or the sub-scale, RL formation may play a critical role in the degradation of interconnect performance. These issues were discussed in a recent viewpoint paper by Fergus [17], and it was suggested that the most likely outcome was the formation of $(Mn,Co,Cr)_3O_4$ reaction layers at the chromia/MCO interface. Subsequently, experiments were performed to model these interactions using MCO/Cr_2O_3 diffusion couples with Pt markers at the interface [18]. X-ray diffraction (XRD), scanning electron microscopy (SEM) and energy-dispersive X-ray spectrometry (EDXS) were used to analyze the couples after exposure for 24 h at 1200 °C. It was found that a $(Mn,Co,Cr)_3O_4$ spinel reaction bilayer was formed due to inward diffusion of Mn and Co, and outward diffusion of Cr. These studies also revealed the effects of various transition metal MCO dopants on the rates at which the reaction layers developed. In parallel neutron diffraction studies [19,20] the details of the site occupancies in $(Mn,Co)_3O_4$ and $(Mn,Co,Cr)_3O_4$ spinel structures have been investigated.

Although experiments of the type performed by Fergus et al. give a fundamental insight into the processes that can occur in these systems, detailed microstructural and chemical characterization experiments on real reaction layers formed under long-term SOFC operating conditions will be necessary for the development of the future generations of SOFC interconnect coatings. In our work we have studied Haynes 230 and Crofer22 APU alloys coated with $Mn_{1.5}Co_{1.5}O_4$ and exposed for up to 1000 h at between 700 and 900 °C. We have previously reported SEM/EDXS evidence for the formation of reaction layers in both systems [21] with the reaction layers formed on Crofer22 APU being thicker than those on Haynes 230. It was proposed that the effects of such layers on the oxidation kinetics could be described using a 3-layer oxidation kinetics model based upon an equivalent circuits approach.

In this paper we present the results of a detailed microstructural investigation on the MCO-coated Crofer22 APU samples from our previous study [21]. These samples were examined in the as-coated condition and after exposure times of 250 and 1000 h at 800 °C. Focused ion beam (FIB) cross-sectioning was used to obtain thin samples for transmission electron microscopy (TEM) studies. The chemistries of the various phases in the samples were determined by EDXS in scanning transmission electron microscopy (STEM) mode. It is shown that the reaction layers are rather different from those reported in the literature with spinels forming both at the alloy/chromia and chromia/MCO interfaces. These data are used to infer the mechanisms by which the reaction layers form, and the likely effects of these layers on the overall lifetime and performance of the SOFC stacks are discussed.

2. Experimental

For this study, square coupons (25 mm × 25 mm) were cut from 0.5 mm thick Crofer22 APU commercial sheet stock. The coupon surfaces were prepared by mechanical grinding with successively finer grades of SiC paper and then polishing with 6 μm diamond paste. This procedure was adopted to eliminate any surface defects due to sheet processing and to ensure that all of the coupons had a consistent surface finish. Prior to applying the coatings, any residue from the polishing process was removed by: ultrasonic cleaning in an acetone bath, rinsing with isopropanol, and allowing the coupons to dry.

$Mn_{1.5}Co_{1.5}O_4$ powder purchased from Praxair was used to form a slurry, which was applied to the polished surfaces of the alloy coupons; this was then converted to densified MCO coatings of approximately 5 μm in final thickness using a variant of the process sequence described by Yang et al. [6]. This sequence comprised: drying in an oven at 100 °C for 2 h; reducing in a sealed tube furnace under flowing $Ar/3\%H_2O/2.75\%H_2$ at 850 °C for 4 h; and then re-oxidizing in air at 850 °C for 4 h. Subsequent oxidation experiments were performed on the MCO-coated coupons in a tube furnace under flowing air (1.5 L min^{-1}) at 800 °C for times of up to 1000 h. The oxidation kinetics data for the samples considered here were presented in our previous paper [21].

Microstructural analysis was performed on three of the coupons: one was in the as-coated condition (i.e. after the reduction/oxidation reactive sintering treatment but with no subsequent extended exposure), and the other two had been oxidized for a duration of 250 or 1000 h. Cross-sections through the three coupons were mounted in epoxy, ground mechanically using SiC papers, polished to a 0.25 μm finish using diamond pastes, and then carbon coated. Site-selective TEM sample preparation was performed using a FEI Strata 400 Dual Beam FIB equipped with a flip-stage and an STEM detector for improved final thinning. In-situ platinum deposition was performed in order to protect the surface of the TEM specimen during ion milling. Ga^+ beam currents were reduced iteratively to a value of 9.7 pA during final milling to avoid excessive Ga^+ implantation and beam damage. TEM foils were mounted onto copper Omni grids at 2 corners in order to limit mechanical buckling of the samples during final thinning.

The samples were examined in a Philips CM-200 supertwin equipped with an EDAX 30 mm^2 SiLi EDXS detector and operating at an accelerating voltage of 200 kV. Diffraction contrast images and selected area diffraction patterns (SADPs) were obtained in TEM mode while annular dark field (ADF) images and EDXS data were obtained in STEM mode.

3. Results

3.1. Development of interfacial layers/reaction products

The development of the interfacial reaction products was revealed by comparing STEM imaging and spectrometry data from the as-coated, 250 h and 1000 h samples: representative data are presented in Figs. 1–3, respectively. Fig. 1(a) is an ADF image obtained from the FIB-cut cross-section of the as-coated sample with the alloy on the left-hand side of the image and the MCO coating on the right. Fig. 1(b) is a compositional profile determined from EDXS measurements obtained along the bright horizontal line indicated in Fig. 1(a). Spectra were acquired using a 10 nm spot size at 10 nm intervals along the line with a 3 s integration time at each point. Compositions were extracted from each spectrum using a standard-less quantification of integrated intensities in each of the corresponding K peaks based upon the thin film approximation. The first 2 μm of this profile show a high constant Fe content of

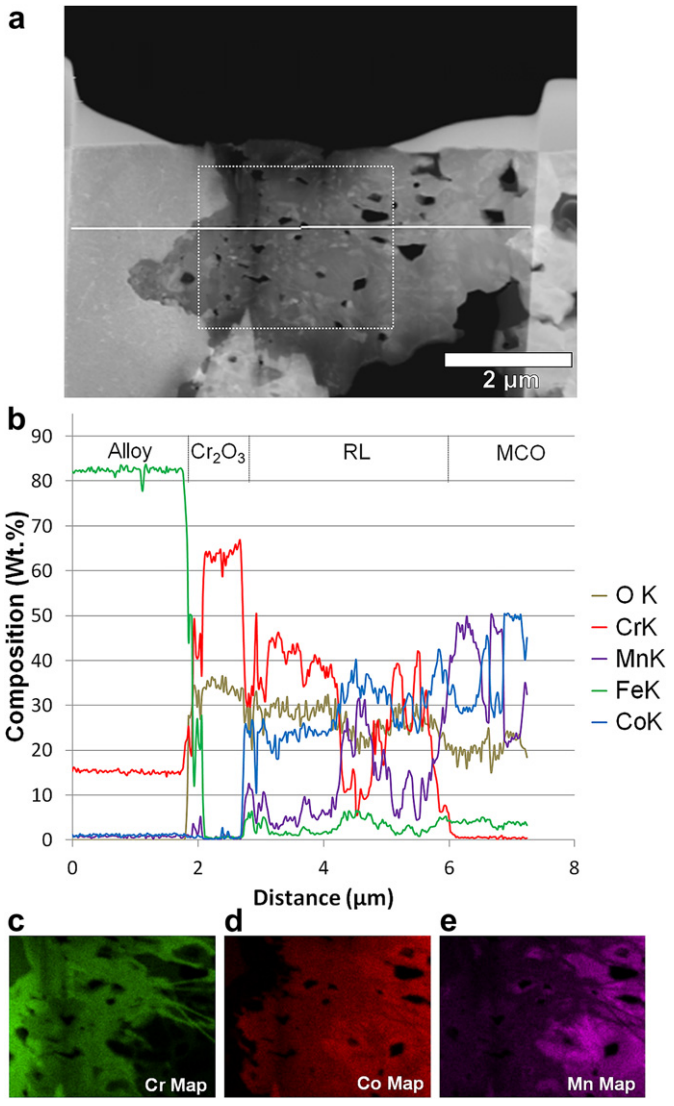

Fig. 1. (a) BF STEM image acquired from a FIB-cut thin cross-section through the as-coated sample. (b) Compositional profile obtained from spectra acquired at points along the horizontal line in (a). (c)-(d) X-ray maps obtained from the area indicated by the dotted box in (a) Using the integrated intensities in 100 eV windows centered on the Kα_1 energies for: (c) Cr, (d) Co and (e) Mn.

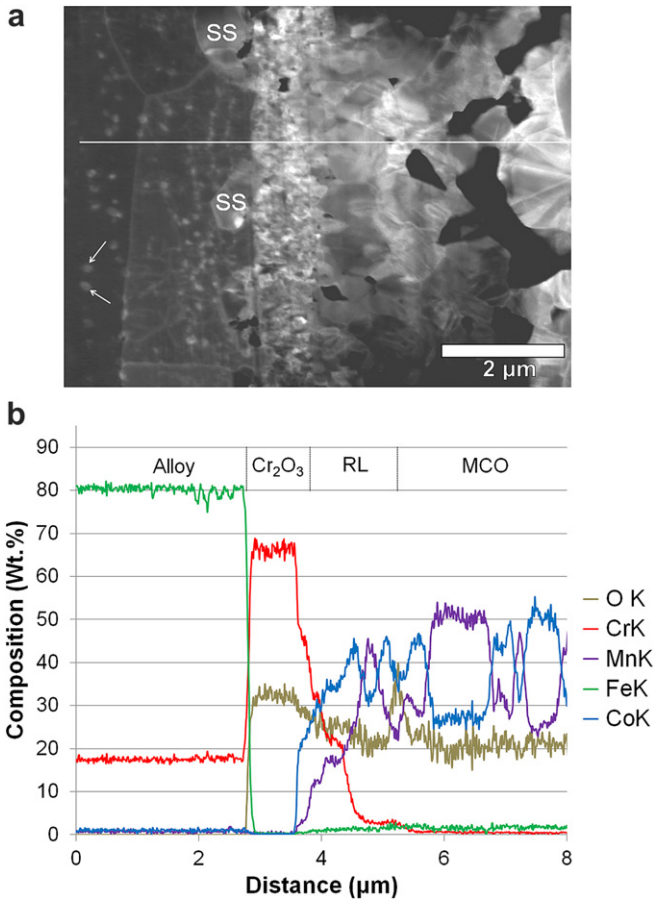

Fig. 2. STEM data acquired from a cross-section through the 250 h sample: (a) BF image; (b) Compositional profile obtained from spectra acquired at points along the horizontal line in (a).

about 82 wt.%, with the balance being comprised of Cr, corresponding to the Crofer22 APU. There is then a band approximately 700 nm wide containing approximately 66 wt.% Cr and 33 wt.% O, as expected for a Cr_2O_3 scale (stoichiometric chromia contains 68 wt.% Cr and 32 wt.% O). Beyond this, there is a band around 3 μm thick which comprises a mixture of O, Cr, Mn and Co in varying proportions. We designate this layer the Reaction Layer (RL). On the left is a region of near constant O content with complementary variations in Mn and Co; this is consistent with what one would expect for an MCO coating with average composition $Mn_{1.5}Co_{1.5}O_4$, which should give roughly equal proportions of Mn_2CoO_4 and $MnCo_2O_4$ phases. There is also a low Fe content (2–6 wt. %) present in the RL and MCO layers. We note that while these four layers/regions are broadly representative of the data obtained from the as-coated samples, the thicknesses of the chromia scale and the RL varied significantly with location along the interface.

The distributions of the various elements in the RL were revealed more clearly in X-ray mapping experiments and a selection of these data is shown in Fig. 1(c) and (e) for Cr, Co and Mn, respectively. These maps were obtained from the region delineated by the 3.25 × 2.6 μm box marked on the ADF STEM image (Fig. 1(a)) and they are shown at the same scale. Each map corresponds to a grid of 256 × 200 measurements of the counts within a 100 eV window centered on the Kα_1 energy for that element. The data were acquired by scanning the region 2048 times with a dwell time of 0.2 ms per measurement for a total acquisition time of around 5.8 h corresponding to just over 0.4 s per pixel. The darker region in the upper left corner of the Cr map is the edge of the Crofer22 APU substrate and the bright band down the left-hand edge of this map corresponds to the chromia scale. Just beyond this is a broader region that is enriched in Cr and Co but not Mn, and on the right-hand side is a region enriched in Co and Mn but not Cr: this latter region corresponds to the MCO. The interfaces between the three oxide regions are very rough, particularly for the Cr/Co-rich and MCO regions wherein the former appears to penetrate into the latter. Indeed there are some thin Cr/Co-rich bands around MCO grains/domains extending to the right-hand side of the mapped region. It is presumably this complex distribution of the Cr/Co-rich and MCO regions that leads to the compositional variations observed in the RL in Fig. 1(b).

A more clearly defined structure comprising layers of more consistent thickness was evident in the STEM data from the 250 h sample (Fig. 2). The ADF image in Fig. 2(a) and the compositional profile in Fig. 2(b) were obtained under the same conditions as those for the as-coated sample in Fig. 1. The chromia scale is a little thicker (around 1 μm), but the reaction layer is thinner (1.5–2 μm)

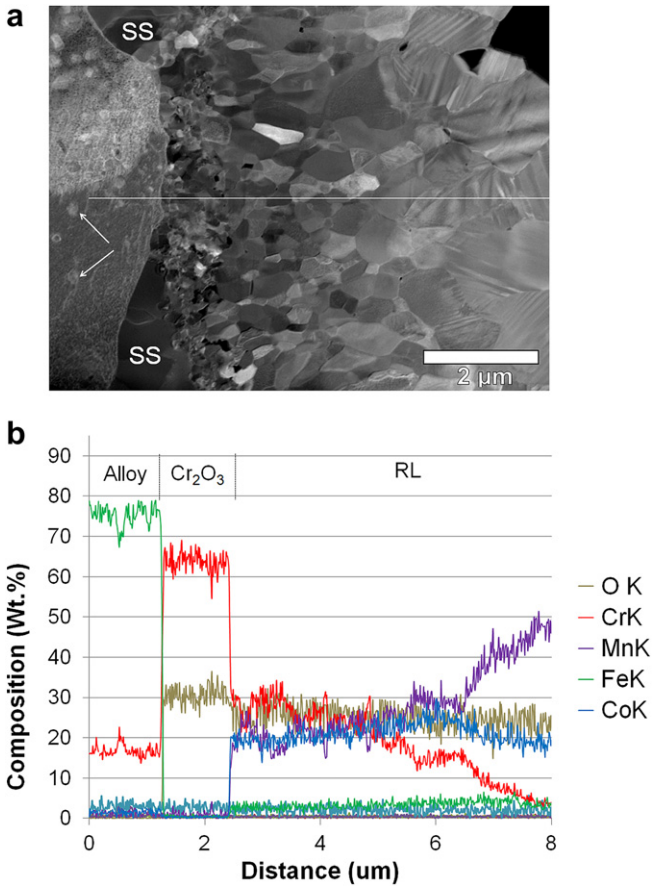

Fig. 3. STEM data acquired from a cross-section through the 1000 h sample: (a) BF image; (b) Compositional profile obtained from spectra acquired at points along the horizontal line in (a).

in this sample than in the as-coated sample. Here again, there are significant fluctuations in the Co, Mn and O contents of the RL, but the Cr content seems to decay steadily with distance from the chromia/RL interface. The Fe contents of the RL and MCO are also lower (1–3 wt. %) in this sample. In addition to these features, we note that there were Ti-rich particles that range from 100 to 400 nm in diameter within the Crofer22 APU substrate; these can be seen as bright equiaxed features in Fig. 2(a): two examples of such features are indicated by arrows in the figure. There are also occasional well-defined pockets of Cr- and Mn-rich sub-scale (SS) oxide at the boundary between the alloy and the chromia scale, and two examples of such pockets are labeled SS in Fig. 2(a).

The corresponding STEM data from the 1000 h sample are shown in Fig. 3. Although the thickness of the chromia scale is similar to that of the 250 h sample at around 1.25 μm, the thickness of the RL is much larger, and it appears that the RL has almost completely consumed the MCO coating in this sample. The transition in Cr content from the chromia scale to the RL is much more abrupt, but thereafter the Cr profile is shallower. Indeed over the first 4 μm of the RL, the variations in the Co, Cr, Mn and O contents are rather gradual with no abrupt compositional changes such as those observed in the RL for the as-coated and 250 h samples. Here again, Ti-rich particles were observed within the alloy below the chromia scale, and well-defined Cr- and Mn-rich SS pockets were observed at the alloy/chromia interface.

The grain structure of the microstructural regions in these samples was revealed more clearly from diffraction contrast effects in axial bright field (BF) TEM images obtained from the FIB-cut samples. One example of such a BF image is shown in Fig. 4, which was obtained from the 1000 h sample. The regions corresponding to the alloy substrate, the SS pockets, the Cr_2O_3 scale and the RL are indicated. Such images were used to obtain measurements of the grain sizes in the chromia scale and RL for each sample, and the data are presented in Table 1. These data show that the mean grain sizes in the RL exceed those for the chromia scale by a factor of 3–4 and that these values increase with increasing oxidation time. Too few SS pockets were observed for meaningful mean grain diameters to be extracted from these regions, but it is clear from Fig. 4 that the grains are substantially larger than those in the RL.

3.2. Phase identification

The phases formed by the interaction of the Crofer22 APU and the MCO coating were identified using a combination of SADPs and EDXS spot analyses on the FIB-cut cross sections. Examples of the TEM data obtained for the phase identification are shown in Fig. 5: in each case a BF TEM image is presented together with the corresponding SADP. We note that all of the data shown in Fig. 5 were obtained from the 1000 h sample, which has the largest grain size and gave the most easily interpretable SADPs and EDXS data. No data is presented for the BCC matrix phase of the alloy, or for the cubic $MnCo_2O_4$ and tetragonal Mn_2CoO_4 phases of the MCO coating since these are well established. The data from the small Ti-rich particles in the alloy adjacent to the chromia scale in the 250 h and 1000 h samples have also been omitted from this figure. These particles contained Ti and O at an atomic ratio of approximately 1:2 with up to 5 at.% Cr, and the SADPs indicated that each particle is a single crystal. Although the measured chemistry was consistent with the particles being Cr-doped TiO_2, the zone axis SADPs were not consistent with any of the three known polymorphs of TiO_2 (anatase, brookite or rutile).

Fig. 5(a) is a BF TEM image obtained from an SS pocket at the interface with the Crofer22 APU substrate. This region is clearly distinguished from the darker alloy region on the left-hand side of the image and the fine-grained chromia scale on the right. The corresponding SADP (Fig. 5(b)) is consistent with this being a phase with a face-centered cubic (FCC) lattice (due to the systematic absences) and a lattice parameter of 0.845 nm; the SADP is indexed

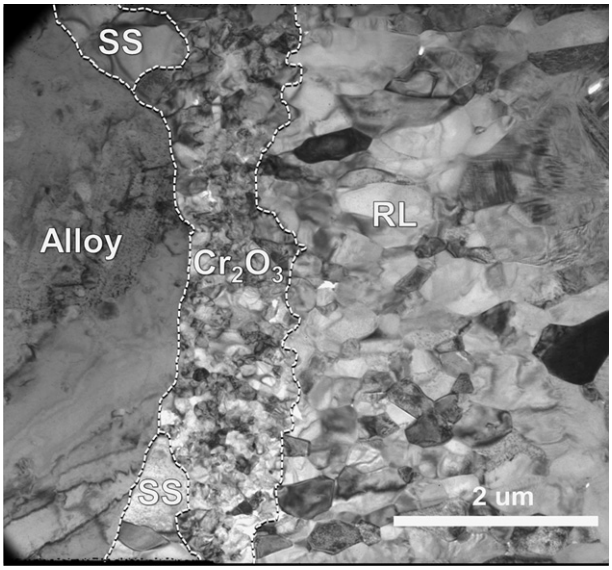

Fig. 4. BF TEM acquired from a cross-section through the 1000 h sample. "SS" denotes pockets of subscale spinel observed between the alloy and chromia scale.

Table 1
Grain sizes measured from TEM cross-section samples for the chromia scale and the $(Mn,Co,Cr,Fe)_3O_4$ spinel RL.

Sample	Chromia grain sizes (nm)		RL spinel grain sizes (nm)	
	Range	Mean	Range	Mean
As-Coated	35–102	72	180–486	273
250 h	35–213	103	141–468	335
1000 h	42–467	163	201–1235	473

on this basis and corresponds to a <112> zone axis pattern. The EDXS data from this pocket showed that the SS contained only Mn, Cr and O at an atomic ratio of exactly 1:2:4. The same result was obtained from another pocket in this sample and from SS pockets in the 250 h sample, indicating that the SS pockets consist of stoichiometric grains of the cubic spinel phase $MnCr_2O_4$ ($a_0 = 0.844$ nm [24]) in both samples.

Fig. 5(c) and (d) are a BF TEM image and a corresponding SADP from the chromia layer. The grains were too fine to obtain single

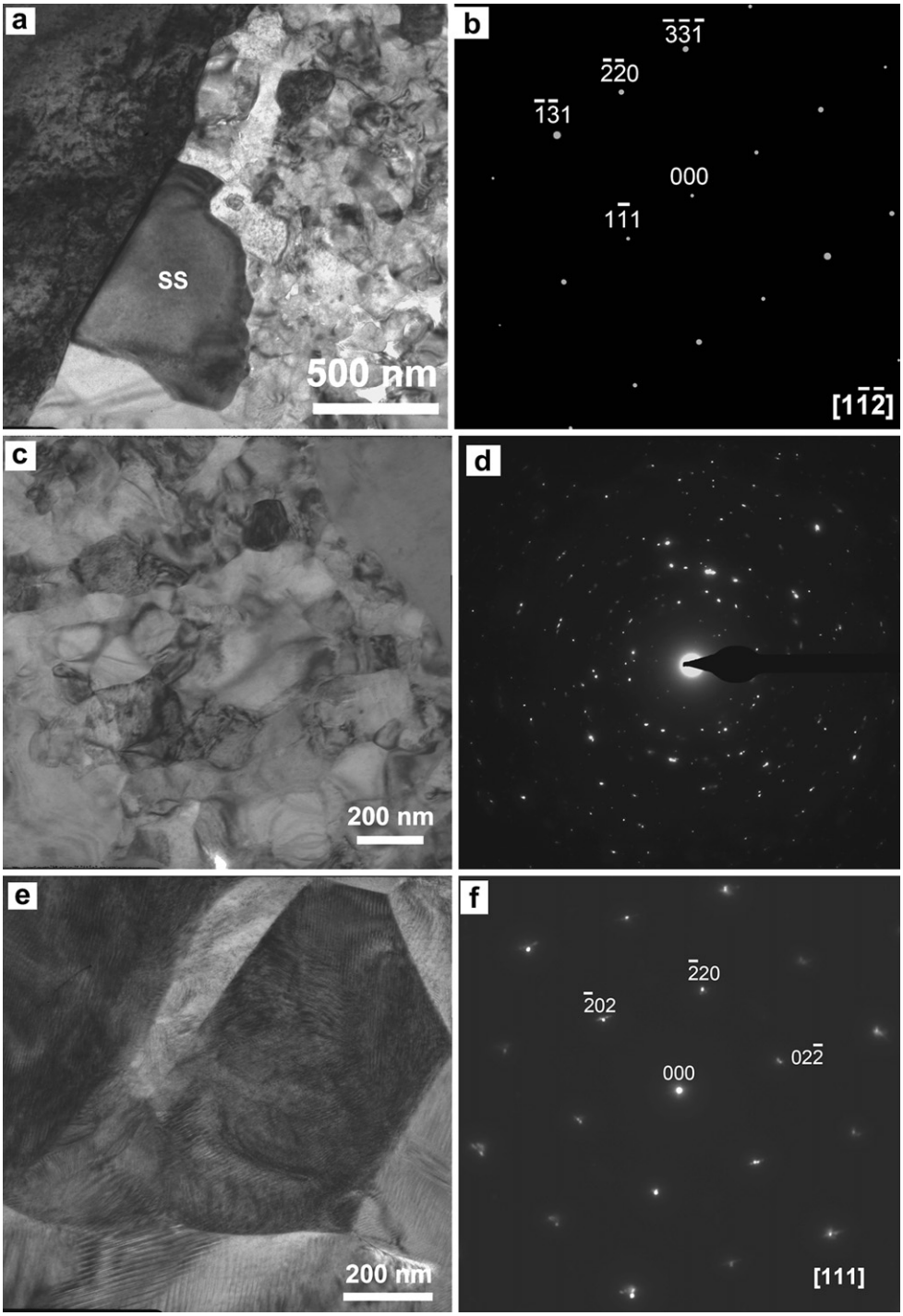

Fig. 5. TEM data acquired from the following microstructural layers in a cross-section through the 1000 h sample: (a) and (b) SS pocket, (c) and (d) Chromia scale, (e) and (f) RL. The SADPs in (b), (d) and (f) were obtained from the regions in the center of the areas shown in the BF TEM images (a), (c) and (e), respectively.

crystal zone axis SADPs but all of the spots in Fig. 5(d) lie on the rings expected for Cr_2O_3 with the corundum structure ($a_0 = 0.496$ nm, $c_0 = 1.359$ nm), as anticipated from the EDXS line-scan data (Fig. 3). The EDXS point analyses performed are consistent with this being stoichiometric Cr_2O_3; the only other species present are Ti and Fe at a total impurity content of less than 0.5 atomic%.

Fig. 5(e) is a BF TEM image showing a large grain in the RL. The corresponding zone axis SADPs were consistent with this being a grain of a cubic spinel phase with a lattice parameter of 0.845 nm, i.e. the same as for the SS $MnCr_2O_4$. One example is shown in Fig. 5(f), which is a [111] zone axis pattern. The EDXS data obtained from this region show that the RL grains contain Mn, Co, Cr and Fe; these cations are not present in simple ratios, and the measured concentrations correspond to a spinel composition of $Mn_{1.38}Co_{0.84}Cr_{0.54}Fe_{0.24}O_4$. There was very little evidence for any grain-to-grain or through-thickness variation in spinel composition from the EDXS data. It is important to note that while we have treated the RL as a cubic spinel in this analysis, there is some subtle splitting of the 220-type reflections in the SADP and very fine ($\approx$5 nm wide) periodic contrast within the RL grains in the BF TEM image. These features may indicate the onset of a transformation from the cubic phase to a lower-symmetry phase upon cooling.

The diffraction data obtained from the RL grains in the 250 h and as-coated samples were also consistent with a cubic spinel phase, although the lattice parameters were slightly smaller at 0.826 and 0.838 nm, respectively. The mean compositions of these RL grains in the scanned areas were obtained from the EDXS data and converted to a spinel formulation in the same manner as for the 1000 h sample; the values obtained were $Mn_{0.79}Co_{1.38}Cr_{0.80}Fe_{0.03}O_4$ and $Mn_{0.33}Co_{0.94}Cr_{1.57}Fe_{0.16}O_4$, respectively. We note that there was far more grain-to-grain variation in spinal composition in these cases, particularly for the as-coated sample.

4. Discussion

4.1. Comparison with previous microstructural studies

The main microstructural features observed in the present work are broadly consistent with those reported in previous studies on MCO-coated Crofer22 APU and on some related systems.

Firstly, there is the formation of a continuous chromia scale between the alloy and the MCO coating. This is consistent with previous studies on MCO-coated ferritic stainless steels (e.g. [8]) including Crofer22 APU, and indeed it is the inhibition of chromia growth and/or confinement of chromia to the alloy/coating interface that is the primary purpose of the coating.

Secondly, there is the presence of the oxide RL corresponding to the interaction of the chromia and the MCO coating. This RL was detected in our previous studies on MCO-coated Crofer22 APU [21], and is anticipated on the basis of results from chromia-MCO diffusion couples [18]. We note however that other studies on MCO-coated Crofer22 APU have reported no incorporation of Cr into the MCO layer even after extended exposure at 800 °C [14]. One possible explanation for this discrepancy is the difference between the spatial resolution for chemical microanalysis in the SEM used in these studies and that in the TEM used here. The spatial resolution of EDXS-based microanalysis in SEM is typically no better than 1 μm, and so it is possible that a narrow RL might not be detected by this technique.

Similar arguments can be used to explain the apparent differences between the MCO compositional profiles presented here and those reported elsewhere. Profiles obtained from MCO using EDXS in SEM typically show a fairly constant composition (e.g. [8,14,21]), whereas XRD data show clearly that the $Mn_{1.5}Co_{1.5}O_4$ composition comprises a mixture of cubic $MnCo_2O_4$ and tetragonal Mn_2CoO_4 spinel phases [8]. The data in Figs. 1(b) and 2(b) show clearly that the grains/domains of the phases are less than 1 μm in diameter; thus an EDXS measurement of the composition in an SEM will sample both phases giving an average MCO composition, whereas the TEM has a microanalytical resolution of around 20 nm under the conditions used here and the constituent phases are resolved clearly.

The main differences between the observations presented here and those in the literature relate to the features on the alloy side of the chromia scale and to the character of the RL. In the 250 h and 1000 h samples we observed SS pockets at the alloy/chromia interface and internal oxides within the Crofer22 APU below the chromia. The SS pockets were identified unambiguously as stoichiometric cubic $MnCr_2O_4$ spinel. The internal oxides had a chemistry corresponding to Cr-doped TiO_2, although the diffraction data were not consistent with any known polymorph of titania. There have been no previous reports of such SS pockets or internal oxides for MCO-coated samples. We note, however, that $MnCr_2O_4$ is the phase that forms on the *exposed* surface of uncoated Crofer22 APU during elevated temperature oxidation in air [22]. Moreover, there have been reports of "Mn-rich intrusions" at the alloy/chromia interface and "TiO_2 precipitates" in cross-sectional SEM studies of a different ferritic stainless steel with a very similar composition after oxidation of uncoated samples for 6000 h at 800 °C in air [23], although no details of the phase identification were provided. The formation mechanism of these $MnCr_2O_4$ pockets is not yet well understood; further experiments on uncoated systems are needed in order to ascertain whether this is an inherent feature of the alloy or a reaction product formed between the alloy and coating.

More significantly, the observations presented here on the RL show dramatic changes in the morphology and character of the spinel, and these findings differ significantly from what is reported elsewhere. Recent work on MCO/chromia diffusion couples [18] has shown that diffusion of Mn and Co into the Cr_2O_3 and concurrent Cr diffusion into the MCO results in a spinel reaction bilayer with $(Mn,Co,Cr)_3O_4$ on the MCO side and $(Mn,Co)Cr_2O_4$ on the chromia side. In our samples we observe essentially only a single spinel RL between the MCO and the chromia. In the as-coated sample this RL is roughly 3 μm thick, penetrates into the MCO coating above, and is enriched in both Cr and Co (Mn:Co:Cr $\approx$ 1:3:5). The 250 h sample exhibits a more compact (1.5–2.0 μm thick) well-defined RL that is Co-rich (Mn:Co:Cr $\approx$ 4:7:4). In the 1000 h sample, however, the RL is thicker (>4 μm) and is Mn-rich (Mn:Co:Cr $\approx$ 7:4:3). Possible ways in which this complex sequence of RL spinels could develop are discussed below.

4.2. Microstructural development during coating and high temperature exposure

When considering the development of the coating microstructure, it is informative to compare the way in which the Cr distribution changes. Fig. 6 is an overlay of the Cr profiles for the as-coated, 250 h and 1000 h samples extracted from Figs. 1(b), 2(b) and 3(b), respectively. For the purposes of comparing the profiles, the position of the abrupt Crofer22 APU/chromia interface was identified as the point where the Fe and Cr contents are equal in each case, and the Cr profiles were then displaced to $x = 0.5$ μm. It is important to note that this is the final position of the Crofer22 APU/chromia interface, not the original position of the Crofer22 APU substrate surface, although the two positions will not vary dramatically because the overall oxidation rate of this coated system is very low. Two important features emerge from this figure. Firstly, there is very little thickening of the chromia scale: the chromia is around 0.7 μm in the as-coated sample, and this rises to

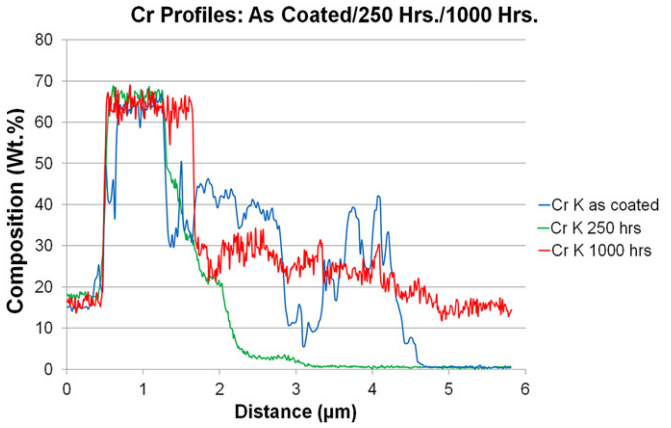

Fig. 6. Overlay of the Cr compositional profiles from Figs. 1(b), 2(b) and 3(b). In each case these are displaced laterally to give the alloy/chromia interface at 0.5 μm for ease of comparison.

about 1 μm in the 250 h sample and 1.25 μm in the 1000 h sample. Secondly, the Cr profile in the RL shows a complex variation with exposure time. In the as-coated sample the Co/Cr-rich spinel RL extends 3–4 μm into the coating, although the profile is very uneven due to porosity and intergrowth of the RL spinel with the MCO as discussed in Section 3. After 250 h exposure, however, this spinel is replaced by a much thinner (1.5 μm) RL with a lower Cr content. After 1000 h, the spinel RL has thickened to > 4 μm. These data seem to imply that the Cr initially diffuses outwards during the coating process, then inwards during the initial exposure, then outwards again during more extended exposure.

To explain this remarkable sequence of Cr fluxes it is necessary to recall that the as-coated state is the net result of three processing steps: application of the MCO slurry to the bare Crofer22 APU substrate, reduction in a Ar + H_2 + H_2O mixture at 850 °C, and then re-oxidation in air at the same temperature. Yang et al. showed that the reduction step converts the MCO to a mixture of manganous oxide (MnO) and metallic Co [8]. It is the presence of metallic Co between the MnO grains that gives the sintering and densification of the coating during the reduction step, but this could also facilitate the outward diffusion of Fe and Cr, both of which exhibit extensive solid solubility in FCC Co at the reduction temperature. Upon re-oxidation, however, one would expect the mixture of metallic Co + MnO phase to convert back to MCO (or some closely related spinels) with the Mn displacing Cr and Fe and causing a reversal of the flux for these species. Once the equilibrium Mn concentration had been (re) established in the MCO, however, Cr and Fe might once again diffuse outwards. Using this as a working hypothesis, one could envisage the microstructural development as occurring by the processes depicted in Fig. 7 and described below.

Firstly, the MCO slurry is applied to the Crofer22 APU substrate and dried at 100 °C giving a porous friable green coating of MCO particles held together only by a small volume fraction of polymer binder (Fig. 7(a)). The binder is eliminated during ramping to the reduction temperature, and the MCO particles are then reduced to MnO + Co in the Ar + H_2 + H_2O mixture. We can then account for the as-coated microstructure if there is some preferential redistribution of Co to the alloy/coating interface so that the alloy is in contact with the metallic FCC Co phase. As such, one might expect diffusion of Cr and Fe into the FCC Co-rich metal at the interface (Fig. 7(b)). This process is presumably more rapid for Cr than for Fe due to the differences in the diffusion coefficients. Moreover, given the extensive solubility of Mn in Co at the reduction temperature, it seems likely that the metallic FCC phase will also contain some Mn. During the subsequent re-oxidation, one might expect the reverse processes to occur, i.e. reaction of MnO + Co to form MCO and the concurrent diffusion of Cr and Fe back toward the substrate. If, however, the oxidation front advances more rapidly than the Cr and Fe can diffuse (as one might expect since the diffusivity of O in Co is far higher than that of Cr or Fe), then the cation content of the oxide at the coating/alloy interface would correspond more closely to that of the metallic layer formed during reduction than to that of the starting MCO powder. One would also expect the formation of a compact chromia layer at this interface. These processes would account for the formation of a rather thick Co/Cr-rich and Mn-lean spinel RL between the chromia scale and the MCO (Fig. 7(c)) as observed experimentally for the as-coated sample (Fig. 1). Since the RL in this condition is Mn-lean, the adjacent MCO must be Mn-rich with more Mn_2CoO_4 than $MnCo_2O_4$. If these MCO phases are more stable than the Co/Cr-rich spinel in the RL then during subsequent extended exposures one might expect inward Mn diffusion. The Cr displaced by the Mn could be incorporated into the chromia scale giving a much narrower Cr profile (Fig. 7(d)) as observed for the 250 h sample (Fig. 2). Once the Co/Cr-rich spinel has been consumed, subsequent reactions may be mediated by the chromia scale in the manner discussed by Fergus et al. [17,18] wherein the chromia is simultaneously consuming the alloy while it is being consumed by the diffusion of Mn and Co to form a reaction layer (Fig. 7(e)). This is consistent with our results, which show that the chromia scale thickness is not increasing significantly over the time periods considered here. The consumption of the chromia at the interface with the coating would result in the re-incorporation of Cr into the spinel phases establishing a Cr-modified RL as observed for the 1000 h sample (Fig. 3). The absence of any significant compositional fluctuations in this layer (as compared to the co-ordinated modulations in Co and Mn in the Cr-free MCO) suggests that the Cr in the RL is stabilizing one of these spinel phases over the other.

4.3. Implications for oxidation kinetics and fuel cell performance

To date, most of the SOFC interconnect literature cites the chromia scale thickness as being the main contributor to the development of ohmic losses with exposure time. The current work clearly shows that (Mn, Co, Cr, Fe)$_3O_4$ reaction layers that form even after 1000 h constitute the majority of the interface. Therefore it is not just the conductivity of the chromia scale, but also the conductivity of the spinel reaction layers that form that are critical to achieving long term durability at SOFC operating temperatures. Electrical conductivity values of varying compositions of (Mn, Co, Cr)$_3O_4$ have been reported by Wang et al. [18] and indicate that adding Cr to the MCO spinel structure decreases the conductivity. Spinel pellets of $Mn_{1.25}Co_{1.25}Cr_{0.5}O_4$, $MnCoCrO_4$ and $Mn_{0.4}Co_{0.6}Cr_2O_4$ measured at 800 °C had electrical conductivity values of 22.2 S cm^{-1}, 2.3 S cm^{-1} and 0.009 S cm^{-1} respectively. Chromia conductivity is dominated by defects and measured values vary widely (0.006–0.16 S cm^{-1}). The composition of the spinel reaction layer reported here for the 1000 h sample is similar to the $Mn_{1.25}Co_{1.25}Cr_{0.5}O_4$ case considered by Wang et al. [18] (assuming that Fe substitutes for Co). Thus we might expect the conductivity of this reaction layer to be somewhat lower than that of the starting MCO composition, but still at least two orders of magnitude higher than that of the chromia scale.

Previous work by the current authors proposed an equivalent circuit model to explain differences in weight gain observed between MCO coated Ni-base alloys and MCO coated ferritic stainless steels. The models suggest that the thicker reaction layer formed on the ferritic stainless steels may act as an oxygen diffusion barrier, which slows down the chromia subscale growth. MCO coatings on H230 Ni-base alloys were not as effective at slowing oxidation of the underlying alloy which is presumably due to the

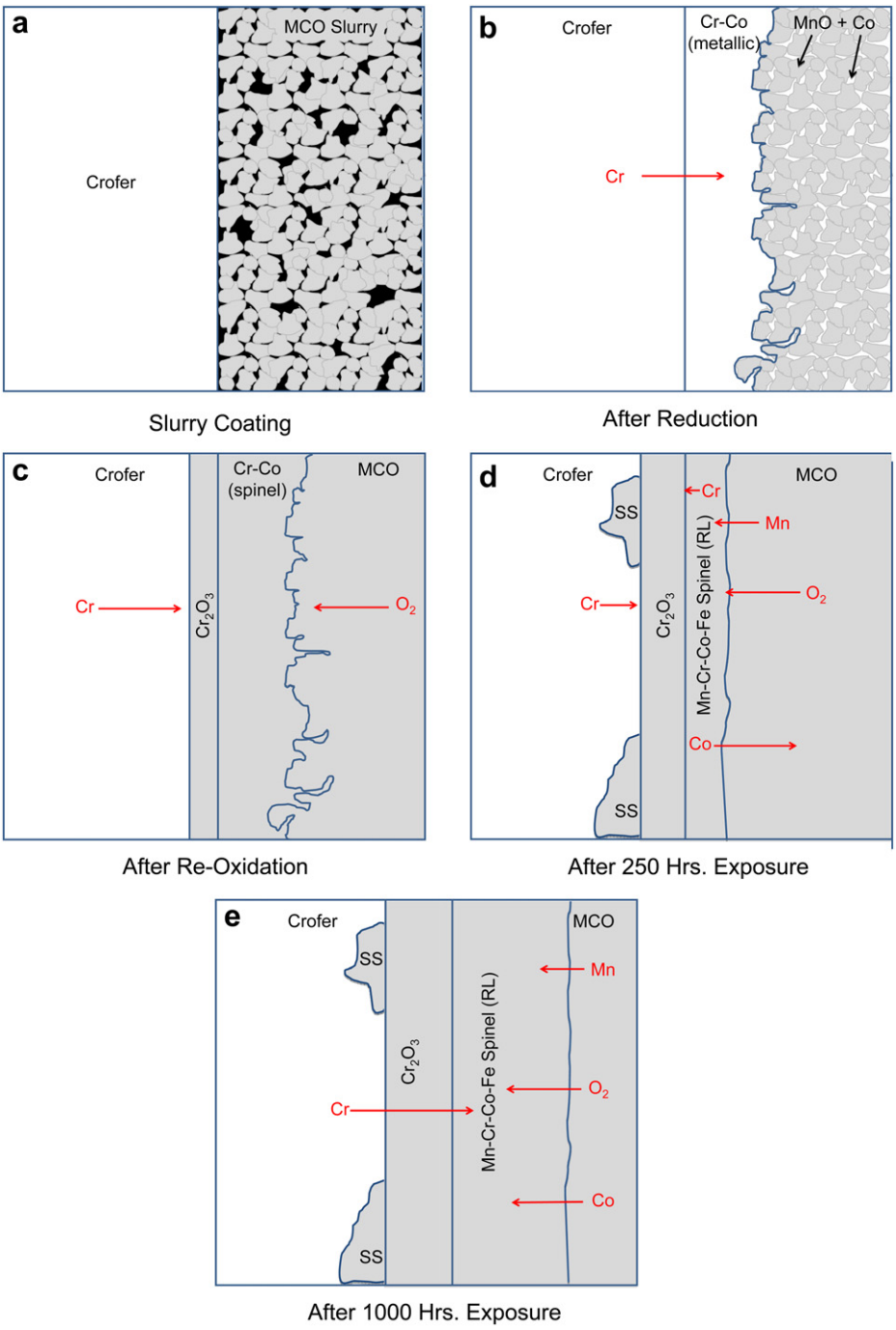

Fig. 7. Schematic diagrams showing the development of microstructural layers and the senses of the associated diffusive fluxes during: (a) application of the MCO slurry; (b) reduction in Ar + H_2 + H_2O; (c) re-Oxidation in air; (d) The initial stages of long-term oxidation; (e) The later stages of long-term oxidation. Oxide phases are shaded gray, metallic phases are white and the black regions in (a) are pores.

much thinner reaction layers formed on these alloys [21]. Thus, it appears as though the reaction layer may have a beneficial effect in terms of limiting chromia scale formation, but does so at the expense of electrical conductivity of the coating. It is expected that after long exposure times, as will be seen in SOFC applications, the MCO coating will be entirely consumed and replaced by a (Mn, Co, Cr, Fe)$_3O_4$ reaction layer.

Subscale spinel pockets of $MnCr_2O_4$ observed in the current work must also be considered a potential degradation mechanism for fuel cell performance for this particular alloy/coating system. The literature suggests that the $MnCr_2O_4$ spinel has an electrical conductivity of 0.004 S cm^{-1} at 800 °C [24]. This phase is therefore highly undesirable from an electrical conductivity standpoint and could potentially contribute to ohmic losses in MCO-coated Crofer22 APU interconnects. In addition to having undesirable electrical conductivity, $MnCr_2O_4$ could potentially cause accelerated degradation due to thermal cycling. $MnCr_2O_4$ has a thermal expansion coefficient (TEC) of 7.47 × 10^{-6} K^{-1} [25] which is lower than the TEC of the Cr_2O_3 and Crofer22 APU (9.6 × 10^{-6} K^{-1} and 11.9 × 10^{-6} K^{-1} respectively) [18,26]. Thus the formation of spinel

RLs could lead to an increased tendency for interfacial delamination or even spallation of the MCO coating during service.

5. Conclusions

Coatings of MCO have been deposited on Crofer22 APU substrates by a slurry process followed by reduction and re-oxidation to promote sintering. Microstructural analysis by TEM and EDXS techniques on FIB-cut cross-sections through as-coated samples and samples after oxidation at 800 °C in air for 250 and 1000 h have revealed the following features:

1. The as-coated samples have a thin (0.7 μm) chromia scale at the alloy/coating interface and a thicker (>3 μm) RL comprising a Co/Cr-rich spinel between the chromia and the MCO. The interface between the RL and the MCO is rather rough and with regions of this spinel penetrating between the MCO grains in the layer above.
2. The 250 h samples have a slightly thicker (1.0 μm) chromia scale but a significantly thinner (1.5–2.0 μm) and more well defined spinel RL. This spinel contains significantly more Mn and Co but less Cr than that in the as-coated sample. There are also internal Ti-rich oxides in the Crofer22 APU below the chromia scale and stoichiometric SS pockets of the cubic spinel $MnCr_2O_4$ at the chromia/alloy interface.
3. The 1000 h samples show very little thickening of the chromia scale, or further development of the SS pockets and internal oxides. The spinel RL is, however, much thicker (>4 μm) with a uniform composition of around $Mn_{1.38}Co_{0.84}Cr_{0.54}Fe_{0.24}O_4$.

We infer that these unusual changes in the thickness, morphology and composition of the spinel RL are related to changes in the diffusive fluxes during the development of the coating microstructure. Thus, the observations can be rationalized if there is: segregation of metallic Co to the coating/substrate interface with outward diffusion of Cr from the alloy in the reduction stage; conversion of the metallic layer to Co/Cr-rich spinel during subsequent re-oxidation; reversion of the Co/Cr-rich spinel to more MCO-like phases during the earlier stages of exposure; and development of Cr-doped MCO-like phases in the RL during subsequent evolution of the chromia layer as oxidation proceeds. These observations could have important consequences for the understanding of degradation mechanisms in SOFC interconnects produced from MCO-coated Crofer22 APU since we anticipate that both the RL spinel and the SS $MnCr_2O_4$ pockets will have lower electrical conductivities than the MCO.

Acknowledgments

The authors would like to thank Dr. J.W. Fergus of Auburn University for helpful discussions. This paper is based in part upon work supported by the National Science Foundation under Grant No. 1100427.

References

[1] H. Kurokawa, C. Jacobson, L.C. DeJonghe, S.J. Visco, Solid State Ionics 178 (2007) 287–296.
[2] M. Stanislowski, J. Froitzheim, L. Niewolak, W.J. Quadakkers, K. Hilpert, T. Markus, L. Singheiser, Journal of Power Sources 164 (2007) 578–589.
[3] C. Collins, J. Lucas, T.L. Buchanan, M. Kopczyk, A. Kayani, P.E. Gannon, M.C. Deibert, R.J. Smith, D.-S. Choi, V.I. Gorokhovsky, Surface & Coatings Technology 201 (2006) 4467–4470.
[4] J. Froitzheim, H. Ravash, E. Larsson, L.G. Johansson, J.E. Svensson, Journal of the Electrochemical Society 157 (2010) B1295–B1300.
[5] R. Trebbels, T. Markus, L. Singheiser, Journal of the Electrochemical Society 157 (2010) B490–B495.
[6] Z. Yang, G.G. Xia, J.W. Stevenson, Electrochemical and Solid State Letters 8 (2005) A168–A170.
[7] Z. Yang, G.G. Xia, G.D. Maupin, J.W. Stevenson, Surface & Coating Technology 201 (2006) 4476–4483.
[8] Z. Yang, G.G. Xia, X.-H. Li, J.W. Stevenson, International Journal of Hydrogen Energy 32 (2007) 3648–3654.
[9] J. Wu, C.D. Johnson, R.S. Gemman, X. Liu, Journal of Power Sources 189 (2009) 1106–1113.
[10] J. Wu, C.D. Johnson, Y. Jiang, R.S. Gemmen, X. Liu, Electrochimica. Acta 54 (2008) 793–800.
[11] M.J. Lewis, J.H. Zhu, Electrochemical and Solid-State Letters 14 (2011) B9–B12.
[12] X. Montero, F. Tietz, D. Sebold, H.P. Buchkremer, A. Ringuede, M. Cassir, A. Laresgoiti, I. Villarreal, Journal of Power Sources 184 (2008) 172–179.
[13] W. Huang, S. Gopalan, U.B. Pal, S.N. Basu, Journal of the Electrochemical Society 155 (2008) B1161–B1167.
[14] Z. Yang, G.G. Xia, Z. Nie, J. Templeton, J.W. Stevenson, Electrochemical and Solid State Letters 11 (2008) B140–B143.
[15] W.N. Liu, X. Sun, E. Stephens, M.A. Khaleel, Journal of Power Sources 189 (2009) 1044–1050.
[16] J.W. Stevenson, G.G. Xia, J.P. Choi, Y.S. Chou, E.C. Thomsen, K.J. Yoon, R.C. Scott, X. Li, Z. Nie, 12th Annual SECA Workshop, Pittsburgh, PA, July 26–28, 2011.
[17] J.W. Fergus, Scripta Materialia 65 (2011) 73–77.
[18] K. Wang, Y. Liu, J.W. Fergus, Journal of the American Ceramic Society 94 (2011) 4490–4495.
[19] H. Bordeneuve, C. Tenailleau, S. Guillemet-Fritsch, R. Smith, E. Suard, A. Rousset, Solid State Sciences 12 (2010) 379–386.
[20] A. Purwanto, A. Fajar, H. Mugirahardjo, J.W. Fergus, K. Wang, Journal of Applied Crystallography 43 (2010) 394–400.
[21] L. Chen, E. Sun, J. Yamanis, N.J. Magdefrau, Journal of the Electrochemical Society 157 (2010) B931–B942.
[22] Z. Yang, J.S. Hardy, M.S. Walker, G.-G. Xia, S.P. Simner, J.W. Stevenson, Journal of the Electrochemical Society 151 (2004) A1825–A1831.
[23] P. Huczkowski, N. Christiansen, V. Shemet, L. Niewolak, J. Piron-Abellan, L. Singheiser, W.J. Quadakkers, Fuel Cell 06 (2) (2006) 93–99.
[24] Z. Lu, J. Zhu, E.A. Payzant, M.P. Paranthaman, Journal of the American Ceramic Society 88 (2005) 1050–1053.
[25] E. Stefan, J.T.S. Irvine, Journal of Materials Science 46 (2011) 7191–7197.
[26] Crofer 22 APU Material Data Sheet 4046, ed. Thyssen Krupp VDM, May 2010.